Relativistic runaway electron avalanche development near the electric field threshold in inhomogeneous air

G. S. Diniz[1], Y. Wada[2], Y. Ohira[3], K. Nakazawa[4], M. Tsurumi[1,5,6]and T. Enoto[1,6]

[1]Department of Physics, Graduate School of Science, Kyoto University, Kitashirakawa Oiwake-cho, Sakyo-ku, Kyoto-shi, Kyoto, 606-8502, Japan.

[2]Division of Electrical, Electronic and Infocommunications Engineering Graduate School of Engineering, Osaka University, 2-1 Yamadaoka, Suita, Osaka, 565-0871 Japan

[3]Department of Earth and Planetary Environmental Science, The University of Tokyo, 7 Chome-3-1 Hongo, Bunkyo City, Tokyo 113-8654, Japan

[4]Kobayashi-Maskawa Institute for the Origin of Particles and the Universe, Nagoya University, Furo-cho, Chikusa-ku, Nagoya, Aichi 464-8601, Japan

[5]Graduate School of Science and Engineering, Aoyama Gakuin University, 5-10-1 Fuchinobe, Sagamihara, Kanagawa 252-5258, Japan.

[6]Extreme Natural Phenomena RIKEN Hakubi Research Team, RIKEN Cluster for Pioneering Research, 2-1 Hirosawa, Wako, Saitama 351-0198, Japan

Key Points:

- A new empirical model quantifies how electron avalanches vanish because of atmospheric density variations with $\sim 10\%$ accuracy.
- The model limits the initial altitude of electron avalanche development for electric field strengths near the avalanche threshold.
- We narrow the possible gamma-ray glow source height range with the new model which is valid through ~ 0.6 to 18 km.

Corresponding author: Gabriel Sousa Diniz, diniz.gabriel.58j@st.kyoto-u.ac.jp

Abstract

Relativistic Runaway Electrons Avalanches (RREAs) development depends on the applied electric field and the environment air density. This dependency controls the RREA exponential growth length scale. The RREA development affects the bremsstrahlung excess occurring due to the passage of charged particles through the thundercloud's electric fields, the gamma-ray glow. We used Monte Carlo simulations to develop an empirical model showing the RREA behavior in a realistic atmospheric density profile. The new formulation shows how the density variation modulates the electron population under electric field strengths near the RREA electric field threshold. The model limits the initial RREA altitude range as a function of the electric field strength. The new model is valid between ~ 0.6 and ~ 18 km, covering the relevant heights to investigate the generation of ground-detected gamma-ray glows.

Plain Language Summary

Thunderclouds are energy sources for trespassing charged particles from cosmic rays. This extra energy gain converts itself into electron avalanches, known as Relativistic Runaway Electron Avalanches (RREAs), and further bremsstrahlung, the gamma-ray glow. This phenomenon relates to electric field strengths close to the RREA requirement. Such electric field requirement is density-dependent. The atmospheric density variations affect avalanche development, resulting in isolated avalanches by imposing limits to the avalanche's initial altitude. We show how RREAs develop in realistic atmosphere density. We present a modification on the characteristic avalanche length under this condition. The initial avalanche altitude is crucial because it completely modifies the density profile trespassed by a descendent electron shower. Finally, we discuss the consequences of isolated RREAs for high-energy emissions and show that the electric field strength constrains the possible initial altitudes for the gamma-ray glow.

1 Introduction

The interaction between charged particles and thundercloud electric fields comprises the primary process of High Energy Atmospheric Phenomena (HEAP) [*Babich*, 2003]. Such interaction requires more investigation despite extensive research through the decades [*Gurevich et al.*, 1992; *Fishman et al.*, 1994; *Torii et al.*, 2002; *Dwyer*, 2003; *Babich et al.*, 2004;

Coleman and Dwyer, 2006; *Tsuchiya et al.*, 2012; *Kochkin et al.*, 2021]. In particular, the gamma-ray glow is minute-long bremsstrahlung emissions with characteristic MeV energy from Relativistic Runaway Electrons Avalanche (RREA) [*Gurevich et al.*, 1992; *Chilingarian*, 2013; *Wada et al.*, 2021]. The RREA electric field threshold is $E_{\rm th}(z) = E_{\rm th0} n_{\rm r}(z)$; where $E_{\rm th}(z)$ is the threshold at a given altitude z, $E_{\rm th0} = E_{\rm th}(0) = 0.284$ MV/m [*Dwyer*, 2003; *Babich et al.*, 2004] the threshold at sea level, and $n_{\rm r}(z)$ the air density at an altitude z relative to the sea level. Recent simulation studies indicate that gamma-ray glows relate to electric field strength, $E_{\rm S}$, close to $E_{{\rm th}(z)}$ [*Sarria et al.*, 2023; *Diniz et al.*, 2023]. Such $E_{\rm S}$ makes the RREA development sensitive to air density variations because the electron multiplication have an initial altitude, $h_{\rm i}$, where $E_{\rm S} > E_{\rm th}(h_{\rm i})$ and reach regions with $E_{\rm S} < E_{\rm th}(h_{\rm i})$.

We present $E_{\rm S}$ normalized by $E_{\rm th0}$ in our analysis for convenience, i.e, $\delta_{\rm E}(E_{\rm S}) = E_{\rm S}/E_{\rm th0}$. Figure 1 shows how the density profile creates vertical regions where the RREA is allowed due to altitude dependency with the vertical distance from source $\Delta h = h_{\rm i} - z$.

The current work investigates RREA development in a realistic atmospheric vertical density profile. It shows the transition between RREA growth and decay related to the electric field strength, $E_{\rm S}$, and the altitude z, see Figure 1. *Diniz et al.* [2022] showed the electrons' spatial range extension at the levels $E_{\rm S} < E_{\rm th}(z)$, in which there is no avalanche but still a longer-lasting high-energy electron population. Now, we evaluate the regime $E_{\rm S} > E_{\rm th}(h_{\rm i})$ transitioning to $E_{\rm S} < E_{\rm th}(z)$ due to the vertical density change. The regime transition is related to gamma-ray glow emissions observed in Japanese winter [*Wada et al.*, 2021] modeled by *Diniz et al.* [2023]. We show in *Diniz et al.* [2023] that $E_{\rm S} \sim E_{\rm th}(z)$ are suitable for the Gamma-Ray Observations of Winter THunderclouds (GROWTH) reports [*Wada et al.*, 2021]. Here, we present the third of our paper series pursuing a theoretical framework for gamma-ray glows. The first one is *Diniz et al.* [2022], and the second paper is *Diniz et al.* [2023]. They are referred here to as paper I and II, respectively. We describe the number of relativistic electrons, $N_{\rm e^-}$, as a function of $E_{\rm S}$, $h_{\rm i}$, and Δh; thus, $N_{\rm e^-} = N_{\rm e^-}(\Delta h, h_{\rm i}, E_{\rm S})$. Finally, we show the physical consequences of the inhomogeneous air density upon RREA and discuss the corollaries regarding gamma-ray glow generation.

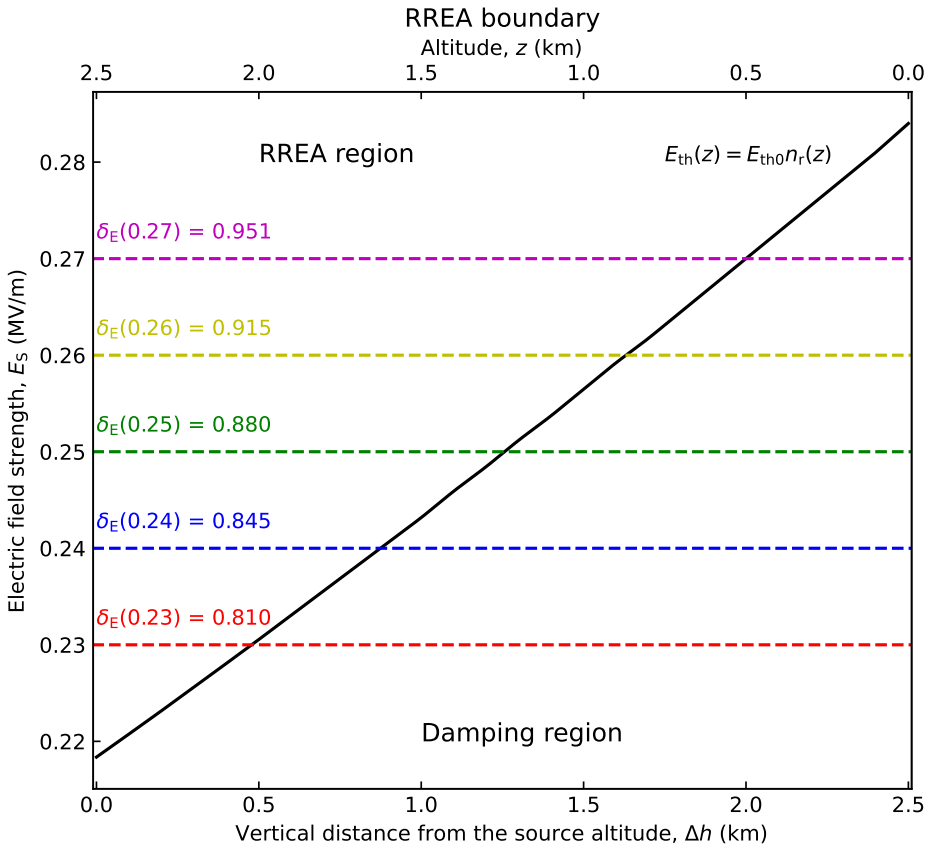

Figure 1. $E_{\mathrm{th}}(z)$ represented as a function of the vertical distance from the source, Δh, (black line) compared with different electric field strength, E_{S}, values represented by the colored dashed lines and translated into electric field strength normalized by the RREA threshold at ground level (E_{th0}), $\delta_{\mathrm{E}}(E_{\mathrm{S}})$. This figure covers the initial altitude, h_{i}, range of 0–2.5 km.

2 Simulation setup and analysis method

Our simulations use GEometry ANd Tracking 4 (GEANT4) version 10.4.3 with the standard "FTFP_BERT_EMZ" physics list [*Agostinelli et al.*, 2003; *Allison et al.*, 2006; *Allison et al.*, 2016] including all the relevant physics. The simulation geometry is a cylinder with a 15 km radius and different heights determined by the number of air layers with different discrete densities following the Naval Research Laboratory Mass Spectrometer Incoherent Scatter radar (NRLMSIS) atmospheric model (`https://kauai.ccmc.gsfc.nasa.gov/instantrun/msis`). We used the standard air composition, which consists of 78.085% nitrogen, 20.950% oxygen, and 0.965% argon. The geometry includes a vertical, upwards homogeneous electric field filling the ambient varying the strength E_{S} between 0.220 and

0.270 MV/m in 0.005 MV/m steps. The electric field is homogeneous and time-constant because existing field measurements in thunderclouds do not provide sufficient data of an accurate $\vec{E}$ profile for our simulation. The air layers have a standard 50 m thickness of different densities. The initial altitude of the point pencil-like electron beam, h_i, varies from 0.75 to 2.50 km in 0.25 km steps. The initial particles are fifty 20 MeV electrons to ensure the avalanche development. The electrons recording are at each interface between two air layers. The simulations include a 100 keV internal energy cutoff for all particles except positrons due to annihilation possibility. We count the electrons with energy above 1 MeV to contribute to the avalanche population and normalize the count by the initial electron number.

Generally, the relativistic electron number, N_{e^-}, depends on the position, $\vec{x}$, the electric field $\vec{E}$ and, the electron kinetic energy ε. The variation with energy can be neglected in the RREA population dynamics since the relativistic electron multiplication process is the Møller scattering. Its cross-section is inversely proportional to the primary particle velocity, $\propto \frac{c}{v_1}$, where c is the speed of light and v_1 the primary electron velocity making the production of relativistic electrons constant as the incoming electron energy increases [*Sarria et al.*, 2018]. Finally, we approximate the position dependency to the vertical direction, z, aligned with the applied electric field.

3 Electron avalanche development as a function of E_S and h_i

The RREA population growth in a homogeneous medium is exponential, $N_{\mathrm{e}^-} \propto e^{z/\lambda_\mathrm{R}(E_\mathrm{S}, n_\mathrm{r})}$, where $\lambda_\mathrm{R}(E_\mathrm{S}, n_\mathrm{r})$ is the characteristic avalanche length defined in Equation 1 in meters [*Dwyer*, 2003] with E_S in MV/m,

$$\lambda_\mathrm{R}(E_\mathrm{S}, n_\mathrm{r}) = \frac{7.3}{E_\mathrm{S} - 0.276 n_\mathrm{r}}\ (\mathrm{m}). \tag{1}$$

Equation 1 shows the decrease of density variations importance if $E_\mathrm{S} \gg 0.276 n_\mathrm{r}$. The atmospheric density profile has a scale height of approximately 8 km [*Köhn et al.*, 2017]. Thus, altitude variations of 1 km correspond to $\sim$ 10% change in density. Such density variations do not alter the RREA dynamics significantly for $E_\mathrm{S} \gg E_\mathrm{th}(z)$. But, the density variations are relevant if $E_\mathrm{S} \sim E_\mathrm{th}(z)$ because the electron population transitions between RREA region and damping regions, see Figure 1. *Sarria et al.* [2023] and paper II relate the latter electric field regime to gamma-ray glows. Thus, understanding the RREA dynamics in this condition is necessary to describe the gamma-ray glow source.

Figure 2 shows the simulated number of electrons with kinetic energy higher than 1 MeV, $N_{e^-}(\Delta h, h_i, E_S)$, versus the vertical distance from the initial altitude, Δh, results for different E_S and h_i, indicated by the legend. Panels A refer to $N_{e^-}(\Delta h, 2\text{ km}, E_S)$ while panels B display $N_{e^-}(\Delta h, h_i, 0.265\text{ MV/m})$.

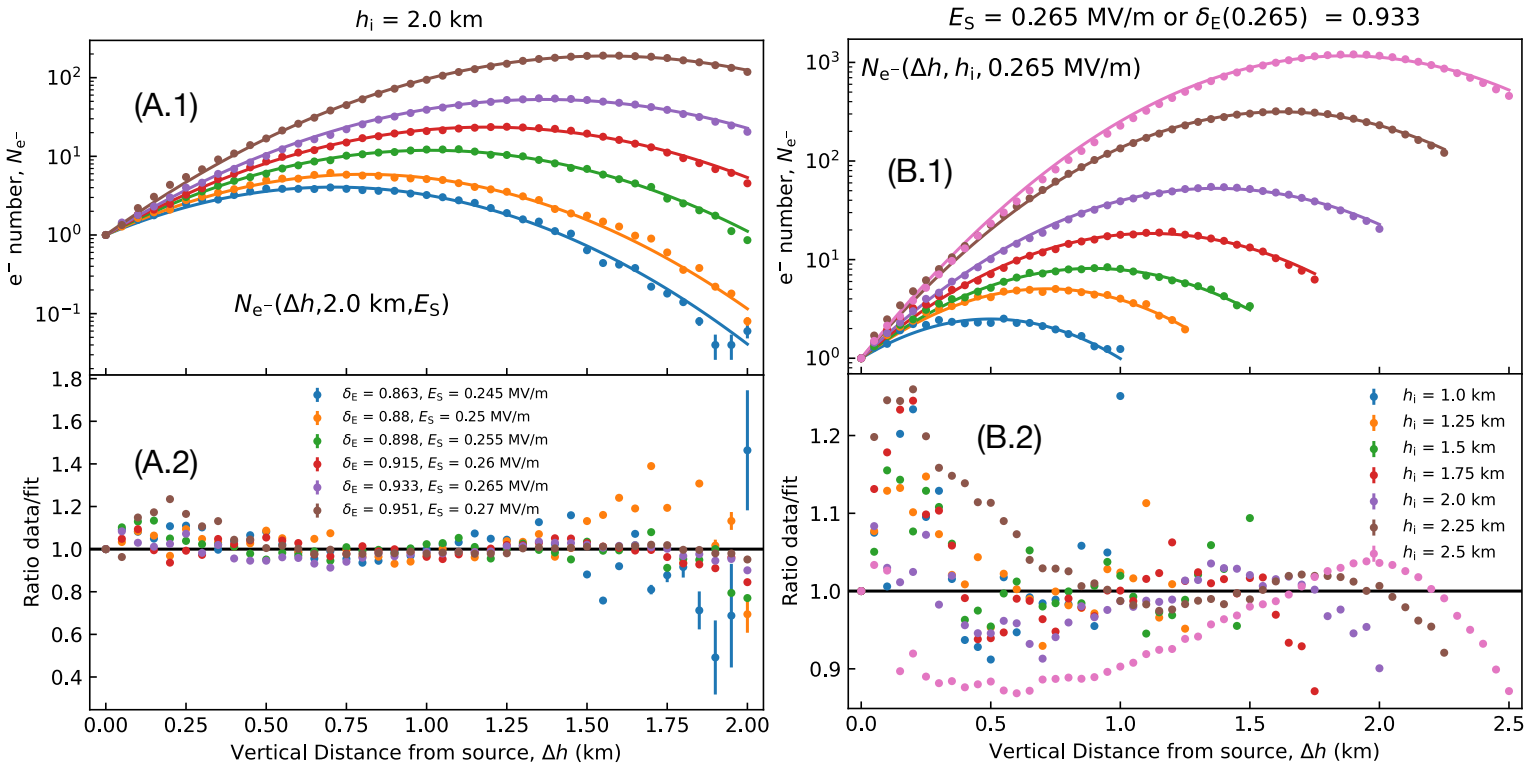

Figure 2. Number of electrons with kinetic energy higher than 1 MeV, $N_{e^-}(\Delta h, h_i, E_S)$, as a function of vertical distance from source, Δh, for different electric field strength, E_S, in panel A.1 and different initial altitude, h_i, in panel B.1 – each one is indicated in the legends. The dots are simulation results, and the curves are fitting models by Equation 2. The error bars follow Poisson statistics as in papers I and II. Panels A.2 and B.2 show the respective data-to-fit ratio.

Equation 2 fits Figure 2 data. The fitting becomes more accurate for increasing E_S due to a better avalanche development for E_S increasingly higher than $E_{th}(h_i)$,

$$N_{e^-}(\Delta h, h_i, E_S) = N_0 e^{\frac{\Delta h}{\lambda_G(E_S,h_i)}\left(1-\frac{\Delta h}{\lambda_D(E_S,h_i)}\right)}. \quad (2)$$

In Equation 2, $\lambda_G(E_S, h_i)$ and $\lambda_D(E_S, h_i)$ are the growth length and damping length, respectively. The fitting constants show $\lambda_G(E_S, h_i)$ and $\lambda_D(E_S, h_i)$ values for each simulation.

In particular, the RREA threshold at 2 km is ~ 0.231 MV/m while the avalanche development starts to be noticeable for $E_S \sim 0.240$ MV/m, in our data set. Stronger electric fields allow RREA development in shorter space. Likewise, the fit quality also improves for increasing h_i, for the same reason as mentioned previously. I.e., an increasing difference between E_S and $E_{th}(h_i)$ at h_i provides a wider space for avalanche development. The regime $E_S \approx E_{th}(h_i)$ requires a larger length than available in the RREA region because of increasing density, see Figure 1. Thus, the RREA does not develop properly, reducing the fitting quality.

The altitude of $N_{e^-}(\Delta h, h_i, E_S)$ maximum, $z_{max}(E_S, h_i)$, can be retrieved by differentiating Equation 2 in respect to Δh, resulting in Equation 3,

$$\Delta h_{max}(E_S, h_i) = \frac{\lambda_D(E_S, h_i)}{2} = h_i - z_{max}(E_S, h_i). \tag{3}$$

Figure 3 shows the dependence of $\lambda_G(E_S, h_i)$, $\lambda_D(E_S, h_i)$, and $\Delta h_{max}(E_S, h_i)$ behavior as a function E_S and h_i, separately. Following Equation 2, $\lambda_G(E_S, h_i)$ must approach $\lambda_R(E_S, n_r)$ for either large E_S and large h_i to recover the exponential growth previously established [*Dwyer*, 2003] because any of these conditions represents the regime $E_S \gg E_{th}(h_i)$.

Figure 3 panels (A.3) and (B.3) display the model accuracy through comparison between the Δh_{max} from fitting (Δh^{fit}_{max}) and data (Δh^{data}_{max}), both normalized by h_i. The convergence of Δh_{max} to h_i shows the RREA better development with an increasing difference between E_S and $E_{th}(h_i)$. Resulting in the approximation of Equation 2 to the already established *Dwyer* [2003] empirical formulation for high E_S or h_i, see Figure 3 panels (A.1) and (B.1).

Combining the electric field strength analysis of Figure 3 (A) with the initial shower altitude evaluation of Figure 3 (B) we reach the multi-variable forms,

$$\lambda_G(E_S, h_i) = B_G - \frac{A_G h_i}{\delta_E(E_S)}, \tag{4}$$

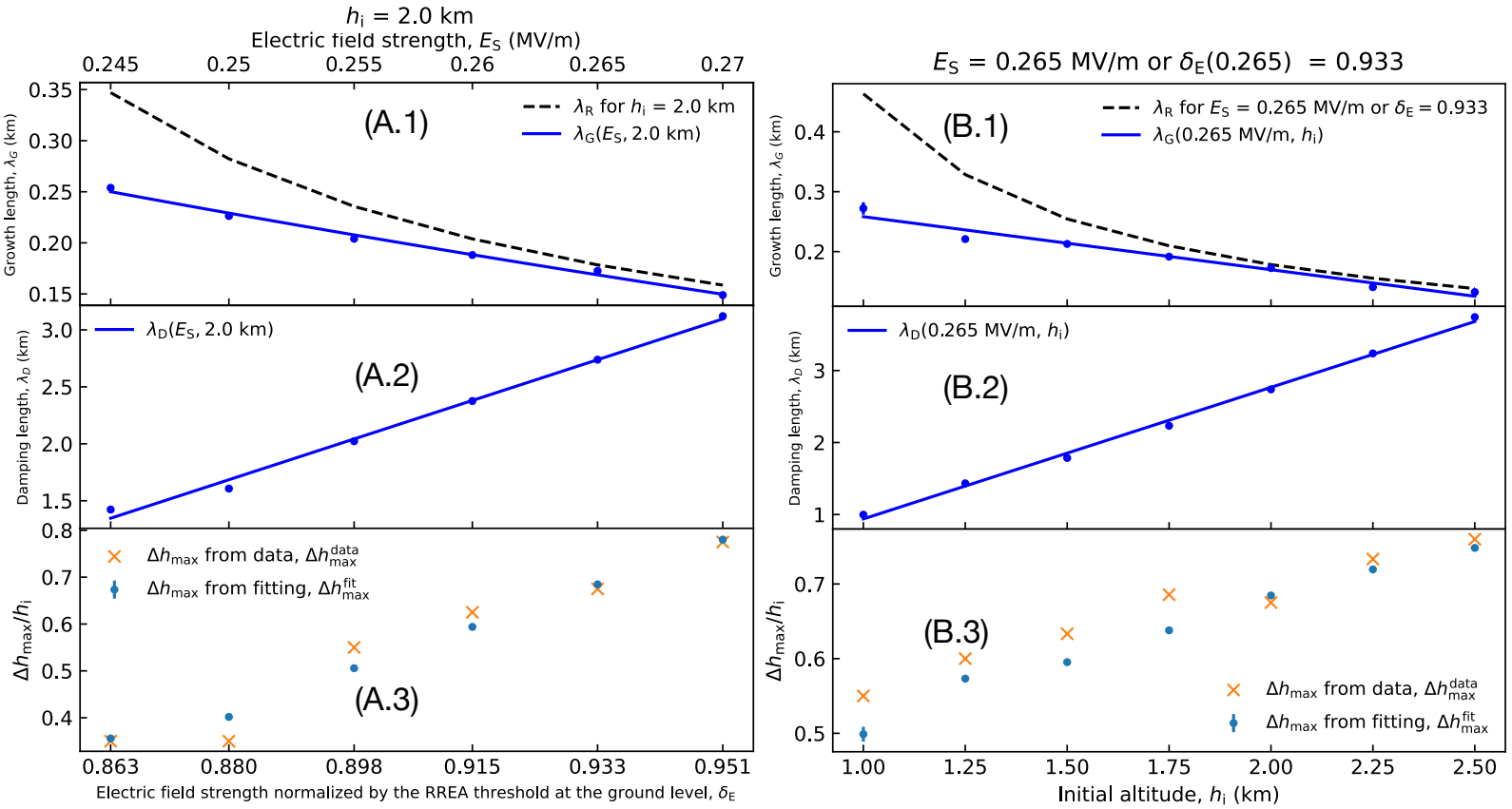

Figure 3. Growth ($\lambda_G(E_S, h_i)$) and damping ($\lambda_D(E_S, h_i)$) lengths, and the vertical distance between the $N_{e^-}(\Delta h, h_i, E_S)$ maximum and the initial altitude, h_i, Δh_{max} (normalized by h_i), as functions of E_S and h_i for the cases in Figure 2. Panels (A.1) and (B.1) compare the respective growth lengths with the characteristic avalanche length, $\lambda_R(E_S, n_r)$. Panels (A.3) and (B.3) compare Δh_{max} retrieved from the data (Δh_{max}^{data}) and retrieved from the fitting (Δh_{max}^{fit}). In panels (A), $\lambda_G(E_S, 2$ km) and $\lambda_D(E_S, 2$ km) are fitted as: $\lambda_G(E_S, 2$ km) = (0.936 ± 0.040)/$\delta_E(E_S)$ - (0.835 ± 0.045) and $\lambda_D(E_S, 2$ km) = (19.872 ± 0.77)$\delta_E(E_S)$ - (15.803 ± 0.699). In panels (B), λ_G(0.265 MV/m, h_i) and λ_D(0.265 MV/m, h_i) are fitted as: λ_G(0.265 MV/m, h_i) = (-0.089 ± 0.008)h_i + (0.347 ± 0.014) and λ_D(0.265 MV/m, h_i) = (1.828 ± 0.048)h_i - (0.889 ± 0.087). The errors are the square root of the covariance matrix diagonal terms.

$$\lambda_D(E_S, h_i) = A_D \delta_E(E_S) h_i - B_D. \quad (5)$$

In Equations 4 and 5, A_i and B_i, with the subindex "i" relative to either growth (G) or damping (D) quantities, are the multi-variable fitting constants. A two variable fitting within

our valid data grid ($E_S > E_{th}(h_i)$ regime) provides, $A_G = 0.014 \pm 0.013$, $B_G = 0.256 \pm 0.030$ km, $A_D = 1.508 \pm 0.241$, $B_D = 0.760 \pm 0.422$ km.

4 Discussion and conclusion

The atmospheric density variation damps the RREA development for electric field strengths close to $E_{th}(h_i)$. The RREA region is smaller than the electric field region because the electron multiplication starts at an altitude of $E_S > E_{th}(h_i)$ and descend to locations where $E_S < E_{th}(z)$. An analog dynamic should be present throughout the thundercloud complex electrical structures such as the thundercloud reactor model [*Stadnichuk et al.*, 2021].

Equations 4 and 5 imposes geometrical limitations upon the Equation 2 model as $\lambda_G(E_S, h_i)$ and $\lambda_D(E_S, h_i)$ need to be positive to have physical meaning. These geometrical limitations are,

$$H_S(E_S) = \frac{B_G \delta_E(E_S)}{A_G}, \tag{6}$$

$$H_I(E_S) = \frac{B_D}{A_D \delta_E(E_S)}. \tag{7}$$

$H_S(E_S)$ and $H_I(E_S)$ are the superior and inferior limits for the initial shower altitude, $H_S(E_S) \geq h_i \geq H_I(E_S)$. The limits $H_S(E_S)$ and $H_I(E_S)$ further constrain the RREA region. And the range of possible RREA initial altitudes reduces as weaker is the electric field because $\lim_{E_S \to 0} H_S(E_S) = 0$ and $\lim_{E_S \to 0} H_I(E_S) = \infty$.

Considering the parameter values found at the end of Section 3, the boundaries for the initial shower altitude from Equations 6 and 7 become $H_S(E_S) = (18.286 \pm 17.114)\delta_E(E_S)$ km and $H_I(E_S) = (0.504 \pm 0.291)/\delta_E(E_S)$ km. The errors result from uncertainty propagation from the fitting parameters. These values are relative to our discrete data grid of E_S and h_i. Thus, a denser data grid will reduce the errors and change the boundaries. In the context of this work, our main interest is in gamma-ray glow ground measurements correlated with winter Japanese thunderclouds [*Wada et al.*, 2021]. Hence, the boundary values cover our purposes.

Figure 4 evaluates the model boundaries and validity. Panel A shows $z_{max}(E_S, h_i)$ from Equation 3 as a function of E_S and h_i. The conditions that limit the model applicability,

$E_{th}(h_i)$, $H_S(E_S)$, and $H_I(E_S)$ are overplotted as dashed lines and mark the region where the present model is valid. The fitting quality may be measured by the difference between Δh_{max} from the data (Δh_{max}^{data}) and from the fitting (Δh_{max}^{fit}) using Equation 3 for the data points that fulfill the condition $E_S > E_{th}(h_i)$.

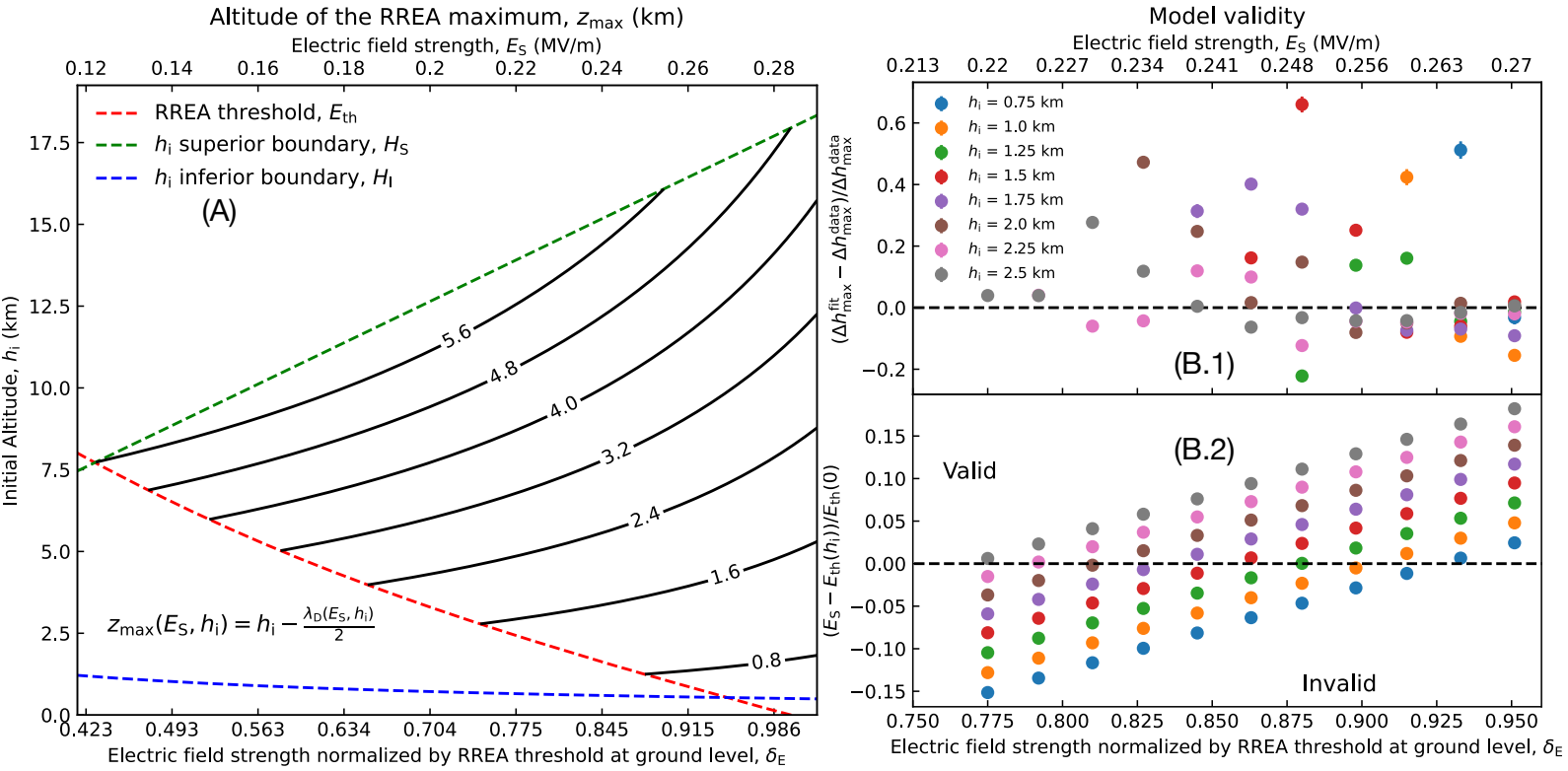

Figure 4. Panel (A) shows the height of avalanche maxima $z_{max}(E_S, h_i)$ as a function of electric field strength E_S and altitude z, displayed by the contour lines with values in kilometers. The dashed red line marks the RREA avalanche threshold, $E_{th}(z)$. The green and blue dashed lines are the model applicability superior and inferior limits $H_S(E_S)$ and $H_I(E_S)$ showing the valid region for the present model, respectively. Panel (B) displays the model validity regarding our discrete data grid. The upper panel (B.1) shows the relative difference between Δh_{max} from the fitting model (Δh_{max}^{fit}) and from the simulated data (Δh_{max}^{data}) as a function of E_S (considering the condition $E_S > E_{th}(h_i)$). The lower panel (B.2) shows the difference between E_S and $E_{th}(h_i)$ normalized by E_{th0}. Each color is for a different h_i indicated by the legend in (B.1).

There are 88 simulated configurations, 52 satisfying the validity condition. Of the 52 valid ones, 69.2% match with the fitting by a 10% difference and 80.7% within a 20% difference. Panel B.1 outliers points show that the data and fitting agreement is sensible to how stronger E_S is than $E_{th}(h_i)$. Panel B.2 shows the normalized difference between the used E_S

and $E_{\rm th}(h_{\rm i})$. The electric field strength, $E_{\rm S}$, must be higher than $E_{\rm th}(h_{\rm i})$ to assure the model applicability, thus, all the configurations above zero are valid.

There are two error sources: (1) the model does not contemplate the particles' horizontal displacement, and (2) the two-dimensional fitting leads to relatively large error bars in comparison to the average values due to the valid data grid shape, see Figure 4 panel (B.2). The error (1) source is negligible as the RREA threshold ($E_{\rm th}(z)$) is a result of the horizontal displacement *Dwyer* [2003]. Error (2) makes the single dimensional fittings of $\lambda_{\rm G}(E_{\rm S}, h_{\rm i})$ and $\lambda_{\rm D}(E_{\rm S}, h_{\rm i})$ (Figure 3) more accurate than the two dimensional fitting (Figure 4). Nevertheless, we show the two-dimensional fitting to visualize the model corollary, $z_{\rm max}(E_{\rm S}, h_{\rm i})$.

Equations 3 and 5 show the $z_{\rm max}(E_{\rm S}, h_{\rm i})$ behavior regarding the electric field strength and the initial altitude,

$$\frac{\partial z_{\rm max}(E_{\rm S}, h_{\rm i})}{\partial h_{\rm i}} = 1 - \frac{A_{\rm D}\delta_{\rm E}(E_{\rm S})}{2}, \tag{8}$$

$$\frac{\partial z_{\rm max}(E_{\rm S}, h_{\rm i})}{\partial E_{\rm S}} = -\frac{A_{\rm D} h_{\rm i}}{2E_{\rm th0}}. \tag{9}$$

Equation 8 shows a global maximum as a function of the electric field strength, $E_{\rm S}$, where $E_{\rm S} = 2E_{\rm th0}/A_{\rm D}$. Considering $A_{\rm D} = 1.508 \pm 0.241$, Equation 8 is positive for $E_{\rm S}$ below $\sim 0.367 \pm 0.060$ MV/m. Thus, $z_{\rm max}(E_{\rm S}, h_{\rm i})$ will increase until $E_{\rm S}$ is enough to well develop the RREA. The fully developed RREA will decrease $z_{\rm max}(E_{\rm S}, h_{\rm i})$ because the electrons are moving downwards and the population maximum will always be the avalanche final point. On the other hand, Equation 9 is always negative regardless $h_{\rm i}$ value. Thus, an horizontal line in Figure 4 panel (A) will present a negative $z_{\rm max}(E_{\rm S}, h_{\rm i})$ rate that decreases with larger $h_{\rm i}$.

There is some freedom on where to consider the initial shower altitude since there is a constant cosmic-ray flux hitting thunderclouds at all times. The initial shower altitude is at the beginning of the electrified space. In the gamma-ray glow framework, This point would be the top of the region between the negative charge center and the lower positive charge center at the cloud base considering the classical tripolar cloud structure [*Takahashi*, 1978; *Williams*, 1989] for ground detection such as [*Wada et al.*, 2021].

Winter thunderclouds in Japan have base altitude of 0.2–0.8 km [*Takahashi*, 1978] which allowed several gamma-ray glow observations [*Torii et al.*, 2002; *Tsuchiya et al.*, 2012; *Wada et al.*, 2019, 2021]. Recently, Paper II reported geometric requirements to explain the gamma-ray glow spectra, reported by *Wada et al.* [2021], considering air with a homogeneous density of ground level. The configurations include three geometric coordinates, acceleration region of vertical length, H_{E}, electric field strength, E_{S} and, an attenuation region of vertical length, H_{a}, making a triad of (E_{S}, H_{E}, H_{a}). The coordinates triad that produces spectra closest to the observations are (0.31 MV/m, 1 km, 0.4 km) and (0.30 MV/m, 0.9 km, 0.3 km).

We must set the equivalent E_{S} to transpose these coordinates to the inhomogeneous air situation. The values, 0.30 and 0.31 MV/m, are 1.056 and 1.091 times the E_{th0}, respectively. The initial shower altitude is $h_{\mathrm{i}} = H_{\mathrm{E}} + H_{\mathrm{a}}$ which means, for the two coordinate sets, 1.2 and 1.4 km. The RREA threshold for these altitudes, $E_{\mathrm{th}}(z)$, is 0.251 and 0.246 MV/m. The equivalent electric field strength for the inhomogeneous air ambient should be $\sim$ 1.056–1.091 times $E_{\mathrm{th}}(z)$ at h_{i} between 1.2–1.4 km. Thus, the gamma-ray glow observations [*Wada et al.*, 2021] are likely correlated with E_{S} ranging from 0.260–0.274 MV/m which is lower than both the estimated values when considering homogeneous air ambient and E_{th0}. Such electric field strength levels produced an isolated and damped RREA determining the gamma-ray glow source region.

The results from Paper II count with a null-electric field regions while the current work considers regions completely filled with electric field. Thus, an analysis dedicated to find the actual electric field strength related with *Wada et al.* [2021] measurements is reserved to future works.

Both evaluations, paper II and the present work, consider homogeneous electric fields within the acceleration region. The electric field may vary in time and space. Such variations would modify the RREA dynamic in reality. Thus, the missing points to resolve the gamma-ray glow process are the electric field accurate geometry and the electric field variation with time inside the thundercloud.

Open research

The simulations of this work use the GEANT4 version 10.4.3 available at, `https://geant4.web.cern.ch`. The data regarding the present analysis is at the dataset *Diniz and Enoto* [2023].

Acknowledgments

This work, G.D. and T.E. are supported by Hakubi Research Project and MEXT/JSPS KAKENHI Grant No. 22H00145, and 22KF0190. Y.W. is supported by KAKENHI Grant No. 22K14453. K.N. is supported by the KAKENHI Grant No. 21H00166. Y.O. is supported by the KAKENHI Grant No. 19H01893 and No. 21H04487. They were done with the RIKEN BIG WATERFALL HOKUSAI computer system.

References

Agostinelli, S., et al. (2003), GEANT4: A simulation toolkit, *Nucl. Instrum. Meth.*, *A506*, 250–303, doi:10.1016/S0168-9002(03)01368-8.

Allison, J., K. Amako, J. Apostolakis, H. Araujo, P. Arce Dubois, M. Asai, G. Barrand, R. Capra, S. Chauvie, R. Chytracek, G. A. P. Cirrone, G. Cooperman, G. Cosmo, G. Cuttone, G. G. Daquino, M. Donszelmann, M. Dressel, G. Folger, F. Foppiano, J. Generowicz, V. Grichine, S. Guatelli, P. Gumplinger, A. Heikkinen, I. Hrivnacova, A. Howard, S. Incerti, V. Ivanchenko, T. Johnson, F. Jones, T. Koi, R. Kokoulin, M. Kossov, H. Kurashige, V. Lara, S. Larsson, F. Lei, O. Link, F. Longo, M. Maire, A. Mantero, B. Mascialino, I. McLaren, P. Mendez Lorenzo, K. Minamimoto, K. Murakami, P. Nieminen, L. Pandola, S. Parlati, L. Peralta, J. Perl, A. Pfeiffer, M. G. Pia, A. Ribon, P. Rodrigues, G. Russo, S. Sadilov, G. Santin, T. Sasaki, D. Smith, N. Starkov, S. Tanaka, E. Tcherniaev, B. Tome, A. Trindade, P. Truscott, L. Urban, M. Verderi, A. Walkden, J. P. Wellisch, D. C. Williams, D. Wright, and H. Yoshida (2006), Geant4 developments and applications, *IEEE Transactions on Nuclear Science*, *53*(1), 270–278.

Allison, J., K. Amako, J. Apostolakis, P. Arce, M. Asai, T. Aso, E. Bagli, A. Bagulya, S. Banerjee, G. Barrand, B. Beck, A. Bogdanov, D. Brandt, J. Brown, H. Burkhardt, P. Canal, D. Cano-Ott, S. Chauvie, K. Cho, G. Cirrone, G. Cooperman, M. Cortés-Giraldo, G. Cosmo, G. Cuttone, G. Depaola, L. Desorgher, X. Dong, A. Dotti, V. Elvira, G. Folger, Z. Francis, A. Galoyan, L. Garnier, M. Gayer, K. Genser, V. Grichine, S. Guatelli, P. Guèye, P. Gumplinger, A. Howard, I. Hřivnáčová, S. Hwang, S. In-

297 certi, A. Ivanchenko, V. Ivanchenko, F. Jones, S. Jun, P. Kaitaniemi, N. Karakatsa-
298 nis, M. Karamitros, M. Kelsey, A. Kimura, T. Koi, H. Kurashige, A. Lechner, S. Lee,
299 F. Longo, M. Maire, D. Mancusi, A. Mantero, E. Mendoza, B. Morgan, K. Murakami,
300 T. Nikitina, L. Pandola, P. Paprocki, J. Perl, I. Petrović, M. Pia, W. Pokorski, J. Que-
301 sada, M. Raine, M. Reis, A. Ribon, A. Ristić Fira, F. Romano, G. Russo, G. Santin,
302 T. Sasaki, D. Sawkey, J. Shin, I. Strakovsky, A. Taborda, S. Tanaka, B. Tomé, T. Toshito,
303 H. Tran, P. Truscott, L. Urban, V. Uzhinsky, J. Verbeke, M. Verderi, B. Wendt, H. Wen-
304 zel, D. Wright, D. Wright, T. Yamashita, J. Yarba, and H. Yoshida (2016), Recent de-
305 velopments in geant4, *Nuclear Instruments and Methods in Physics Research Section A:*
306 *Accelerators, Spectrometers, Detectors and Associated Equipment*, *835*, 186 – 225, doi:
307 https://doi.org/10.1016/j.nima.2016.06.125.

308 Babich, L. (2003), *Highenergy phenomena in electric discharges in dense gases: theory,*
309 *experiment and natural phenomena*, Futurepast Inc., Arlington, Virginia, USA.

310 Babich, L. P., E. N. Donskoy, R. I. Il'kaev, I. M. Kutsyk, and R. A. Roussel-Dupre (2004),
311 Fundamental parameters of a relativistic runaway electron avalanche in air, *Plasma*
312 *Physics Reports*, *30*(7), 616–624, doi:10.1134/1.1778437.

313 Chilingarian, A. (2013), Thunderstorm Ground Enhancements (TGEs) - New High-Energy
314 Phenomenon Originated in the Terrestrial Atmosphere, *Journal of Physics Conference*
315 *Series*, *409*(1), 012019, doi:10.1088/1742-6596/409/1/012019.

316 Coleman, L. M., and J. R. Dwyer (2006), Propagation speed of runaway electron avalanches,
317 *Geophysical Research Letters*, *33*, L11810, doi:10.1029/2006GL025863.

318 Diniz, G., Y. Wada, Y. Ohira, K. Nakazawa, and T. Enoto (2022), Atmospheric elec-
319 tron spatial range extended by thundercloud electric field below the relativistic run-
320 away electron avalanche threshold, *Journal of Geophysical Research: Atmospheres*,
321 *127*(3), e2021JD035,958, doi:https://doi.org/10.1029/2021JD035958, e2021JD035958
322 2021JD035958.

323 Diniz, G. S., and T. Enoto (2023), Relativistic runaway electron avalanche develop-
324 ment near the electric field threshold in inhomogeneous air [dataset], mendeley,
325 http://doi.org/10.17632/czwy2pfhn3.1.

326 Diniz, G. S., Y. Wada, Y. Ohira, K. Nakazawa, M. Tsurumi, and T. Enoto (2023), Ambient
327 conditions of winter thunderstorms in japan to reproduce observed gamma-ray glow en-
328 ergy spectra, *Journal of Geophysical Research: Atmospheres*, *128*(10), e2022JD038,246,
329 doi:https://doi.org/10.1029/2022JD038246, e2022JD038246 2022JD038246.

Dwyer, J. R. (2003), A fundamental limit on electric fields in air, *Geophysical Research Letters*, *30*(20), 2055, doi:10.1029/2003GL017781.

Fishman, G. J., P. N. Bhat, R. Mallozzi, J. M. Horack, T. Koshut, C. Kouveliotou, G. N. Pendleton, C. A. Meegan, R. B. Wilson, W. S. Paciesas, S. J. Goodman, and H. J. Christian (1994), Discovery of Intense Gamma-Ray Flashes of Atmospheric Origin, *Science*, *264*, 1313–1316, doi:10.1126/science.264.5163.1313.

Gurevich, A., G. Milikh, and R. Roussel-Dupre (1992), Runaway electron mechanism of air breakdown and preconditioning during a thunderstorm, *Physics Letters A*, *165*(5), 463–468, doi:10.1016/0375-9601(92)90348-P.

Kochkin, P., D. Sarria, N. Lehtinen, A. Mezentsev, S. Yang, G. Genov, K. Ullaland, M. Marisaldi, N. Østgaard, H. J. Christian, J. E. Grove, M. Quick, S. Al-Nussirat, and E. Wulf (2021), A rapid gamma-ray glow flux reduction observed from 20 km altitude, *Journal of Geophysical Research: Atmospheres*, *126*(9), e2020JD033,467, doi:https://doi.org/10.1029/2020JD033467, e2020JD033467 2020JD033467.

Köhn, C., G. Diniz, and M. N. Harakeh (2017), Production mechanisms of leptons, photons, and hadrons and their possible feedback close to lightning leaders, *Journal of Geophysical Research: Atmospheres*, *122*(2), 1365–1383.

Sarria, D., C. Rutjes, G. Diniz, A. Luque, K. M. A. Ihaddadene, J. R. Dwyer, N. Østgaard, A. B. Skeltved, I. S. Ferreira, and U. Ebert (2018), Evaluation of monte carlo tools for high-energy atmospheric physics ii: relativistic runaway electron avalanches, *Geoscientific Model Development*, *11*(11), 4515–4535, doi:10.5194/gmd-11-4515-2018.

Sarria, D., N. Østgaard, M. Marisaldi, N. Lehtinen, and A. Mezentsev (2023), Library of simulated gamma-ray glows and application to previous airborne observations, *Journal of Geophysical Research: Atmospheres*, *128*(9), e2022JD037,956, doi:https://doi.org/10.1029/2022JD037956, e2022JD037956 2022JD037956.

Stadnichuk, E., E. Svechnikova, A. Nozik, D. Zemlianskaya, T. Khamitov, M. Zelenyy, and M. Dolgonosov (2021), Relativistic runaway electron avalanches within complex thunderstorm electric field structures, *Journal of Geophysical Research: Atmospheres*, *126*(24), e2021JD035,278, doi:https://doi.org/10.1029/2021JD035278, e2021JD035278 2021JD035278.

Takahashi, T. (1978), Riming electrification as a charge generation mechanism in thunderstorms, *Journal of Atmospheric Sciences*, *35*(8), 1536 – 1548, doi:10.1175/1520-0469(1978)035<1536:REAACG>2.0.CO;2.

Torii, T., M. Takeishi, and T. Hosono (2002), Observation of gamma-ray dose increase associated with winter thunderstorm and lightning activity, *Journal of Geophysical Research: Atmospheres*, *107*(D17), 4324, doi:10.1029/2001JD000938.

Tsuchiya, H., K. Hibino, K. Kawata, N. Hotta, N. Tateyama, M. Ohnishi, M. Takita, D. Chen, J. Huang, M. Miyasaka, I. Kondo, E. Takahashi, S. Shimoda, Y. Yamada, H. Lu, J. L. Zhang, X. X. Yu, Y. H. Tan, S. M. Nie, K. Munakata, T. Enoto, and K. Makishima (2012), Observation of thundercloud-related gamma rays and neutrons in Tibet, *Phys. Rev. D*, *85*(9), 092006, doi:10.1103/PhysRevD.85.092006.

Wada, Y., T. Enoto, Y. Nakamura, Y. Furuta, T. Yuasa, K. Nakazawa, T. Morimoto, M. Sato, T. Matsumoto, D. Yonetoku, T. Sawano, H. Sakai, M. Kamogawa, T. Ushio, K. Makishima, and H. Tsuchiya (2019), Gamma-ray glow preceding downward terrestrial gamma-ray flash, *Communications Physics*, *2*.

Wada, Y., T. Matsumoto, T. Enoto, K. Nakazawa, T. Yuasa, Y. Furuta, D. Yonetoku, T. Sawano, G. Okada, H. Nanto, S. Hisadomi, Y. Tsuji, G. S. Diniz, K. Makishima, and H. Tsuchiya (2021), Catalog of gamma-ray glows during four winter seasons in japan, *Phys. Rev. Research*, *3*, 043,117, doi:10.1103/PhysRevResearch.3.043117.

Williams, E. R. (1989), The tripole structure of thunderstorms, *Journal of Geophysical Research: Atmospheres*, *94*(D11), 13,151–13,167, doi:https://doi.org/10.1029/JD094iD11p13151.

Figure 1.

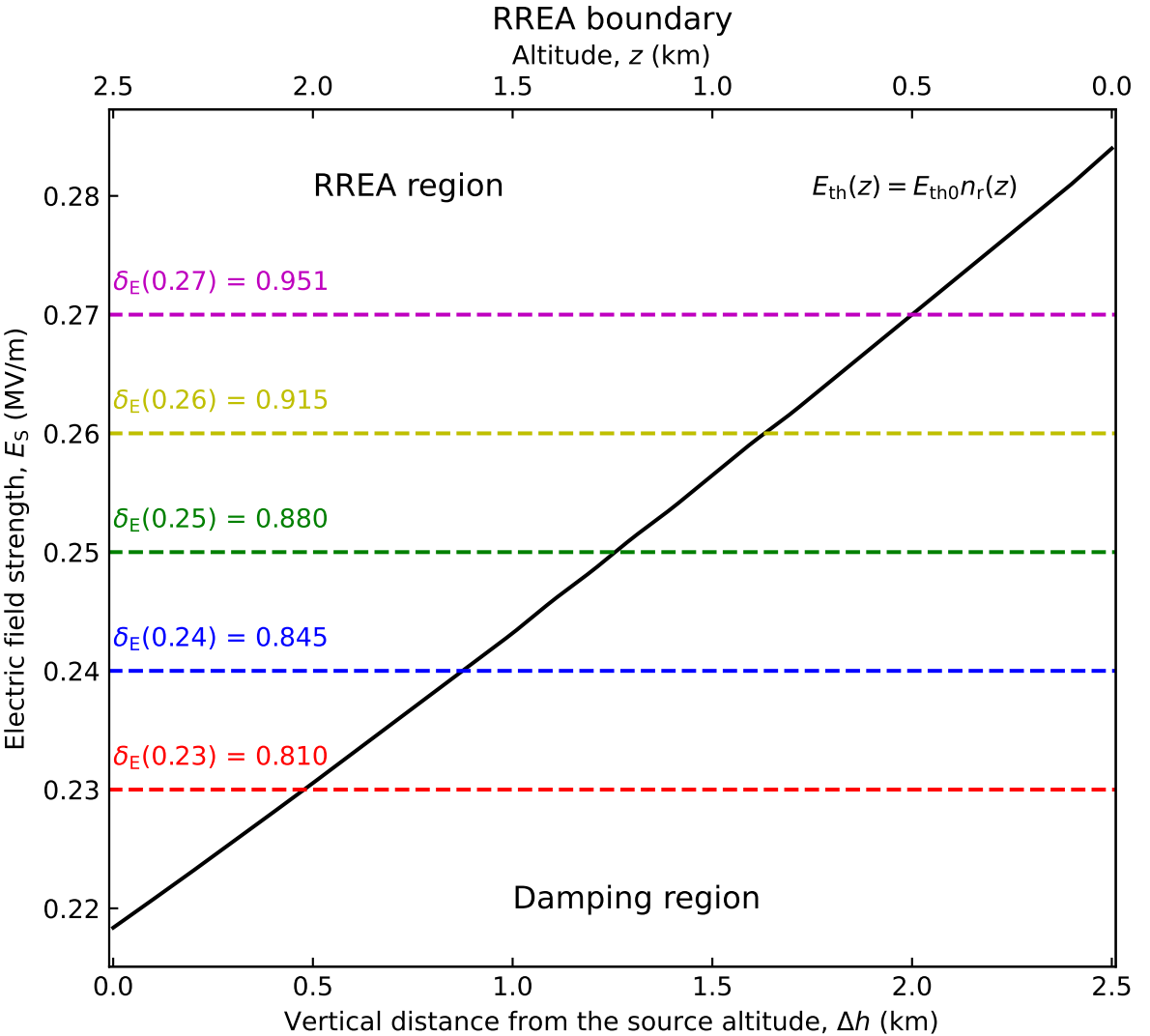
RREA boundary
Altitude, z (km)
2.5
2.0
1.5
1.0
0.5
0.0
RREA region
$E_{th}(z) = E_{th0} n_r(z)$
$\delta_E(0.27) = 0.951$
$\delta_E(0.26) = 0.915$
$\delta_E(0.25) = 0.880$
$\delta_E(0.24) = 0.845$
$\delta_E(0.23) = 0.810$
Damping region
Electric field strength, E_S (MV/m)
0.28
0.27
0.26
0.25
0.24
0.23
0.22
0.0
0.5
1.0
1.5
2.0
2.5
Vertical distance from the source altitude, Δh (km)

Figure 2.

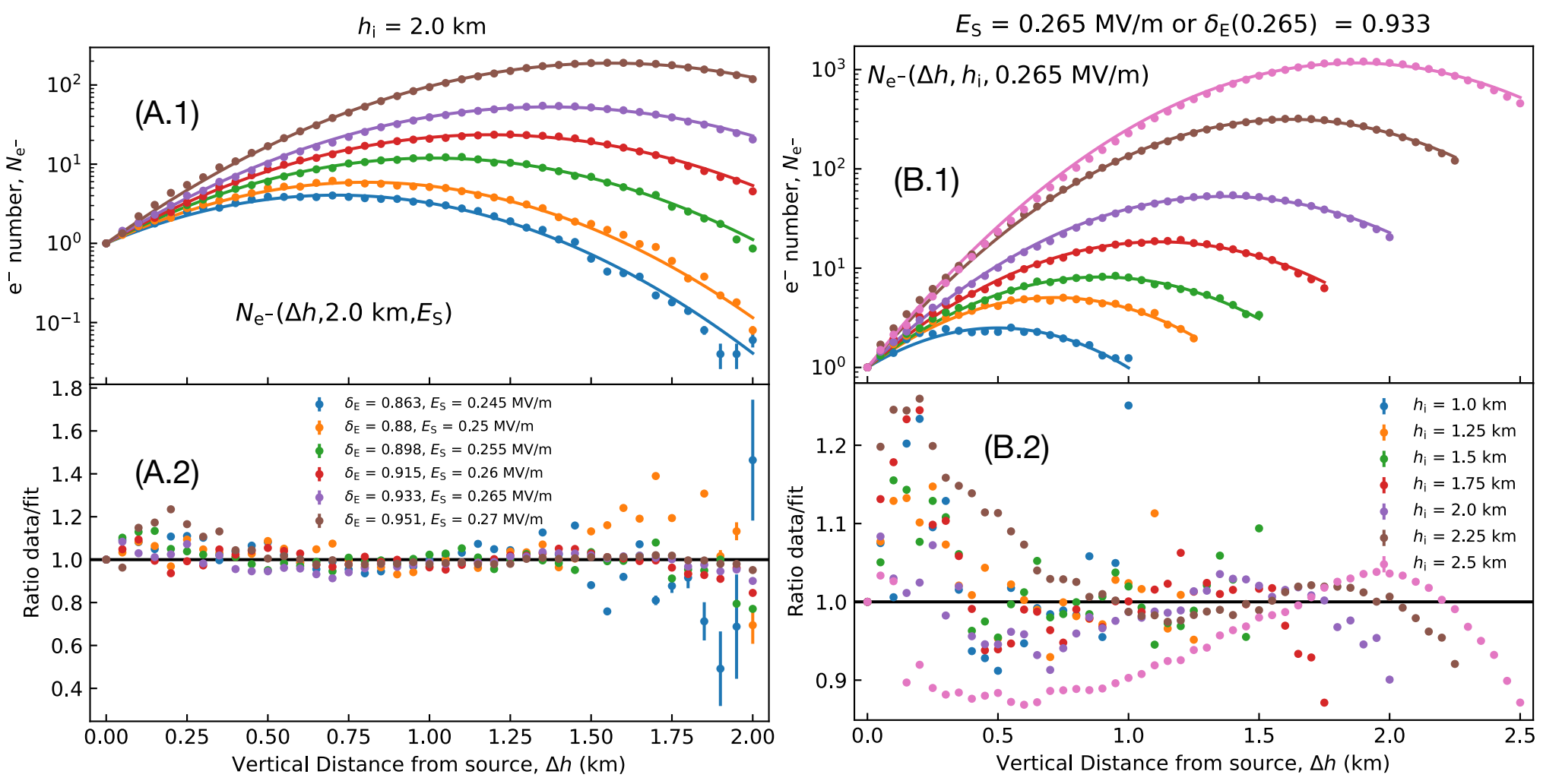
h_i = 2.0 km
E_S = 0.265 MV/m or $\delta_E(0.265)$ = 0.933
(A.1)
N_e-(Δh,2.0 km,E_S)
e⁻ number, N_{e^-}
(A.2)
Ratio data/fit
δ_E = 0.863, E_S = 0.245 MV/m
δ_E = 0.88, E_S = 0.25 MV/m
δ_E = 0.898, E_S = 0.255 MV/m
δ_E = 0.915, E_S = 0.26 MV/m
δ_E = 0.933, E_S = 0.265 MV/m
δ_E = 0.951, E_S = 0.27 MV/m
Vertical Distance from source, Δh (km)
N_e-(Δh, h_i, 0.265 MV/m)
(B.1)
(B.2)
h_i = 1.0 km
h_i = 1.25 km
h_i = 1.5 km
h_i = 1.75 km
h_i = 2.0 km
h_i = 2.25 km
h_i = 2.5 km

Figure 3.

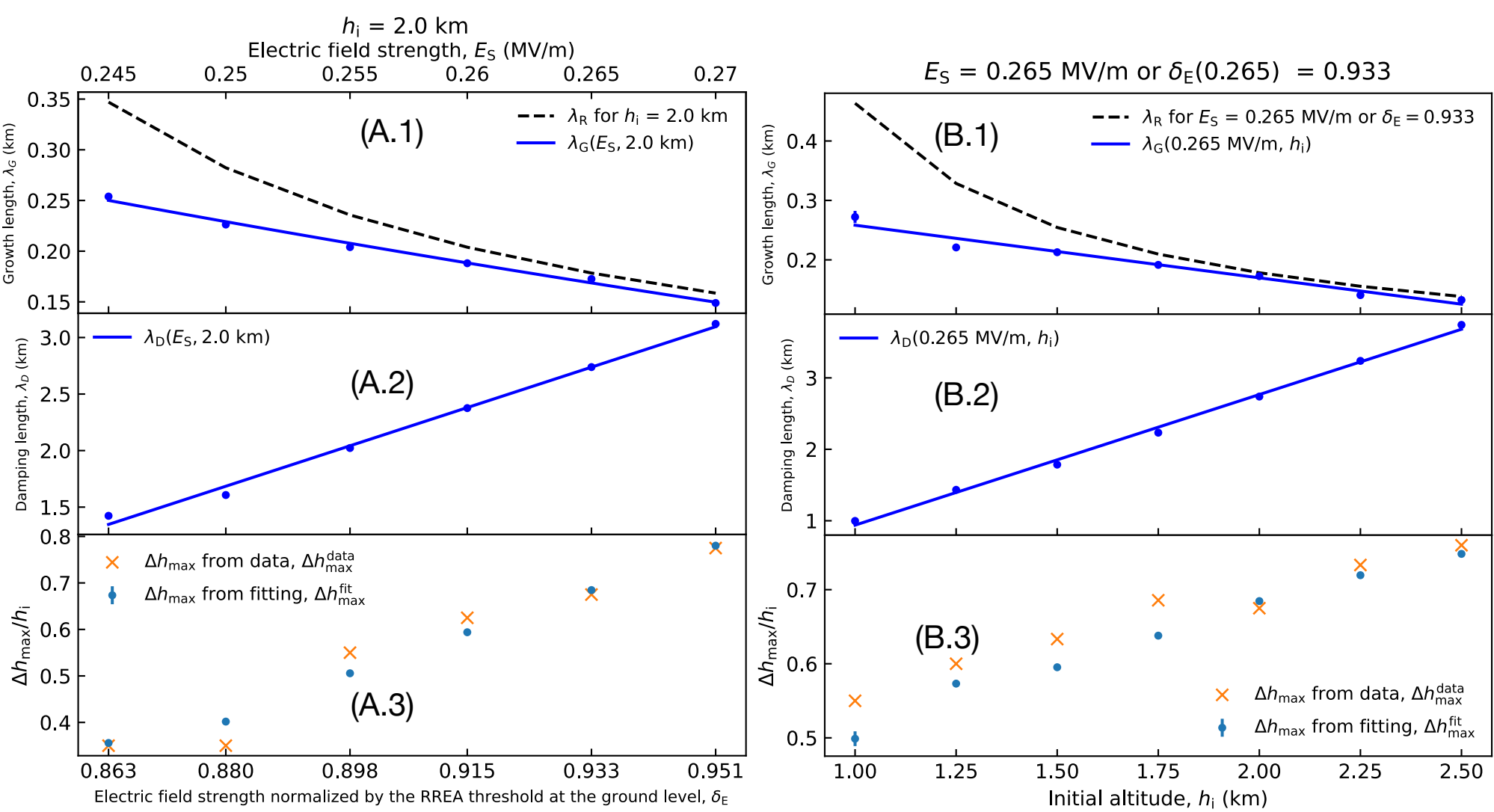
h_i = 2.0 km
Electric field strength, E_S (MV/m)
0.245
0.25
0.255
0.26
0.265
0.27
(A.1)
λ_R for h_i = 2.0 km
$\lambda_G(E_S, 2.0\ km)$
Growth length, λ_G (km)
0.35
0.30
0.25
0.20
0.15
(A.2)
$\lambda_D(E_S, 2.0\ km)$
Damping length, λ_D (km)
3.0
2.5
2.0
1.5
(A.3)
Δh_{max} from data, Δh_{max}^{data}
Δh_{max} from fitting, Δh_{max}^{fit}
$\Delta h_{max}/h_i$
0.8
0.7
0.6
0.5
0.4
0.863
0.880
0.898
0.915
0.933
0.951
Electric field strength normalized by the RREA threshold at the ground level, δ_E
E_S = 0.265 MV/m or $\delta_E(0.265)$ = 0.933
(B.1)
λ_R for E_S = 0.265 MV/m or δ_E = 0.933
λ_G(0.265 MV/m, h_i)
Growth length, λ_G (km)
0.4
0.3
0.2
(B.2)
λ_D(0.265 MV/m, h_i)
Damping length, λ_D (km)
3
2
1
(B.3)
Δh_{max} from data, Δh_{max}^{data}
Δh_{max} from fitting, Δh_{max}^{fit}
$\Delta h_{max}/h_i$
0.7
0.6
0.5
1.00
1.25
1.50
1.75
2.00
2.25
2.50
Initial altitude, h_i (km)

Figure 4.

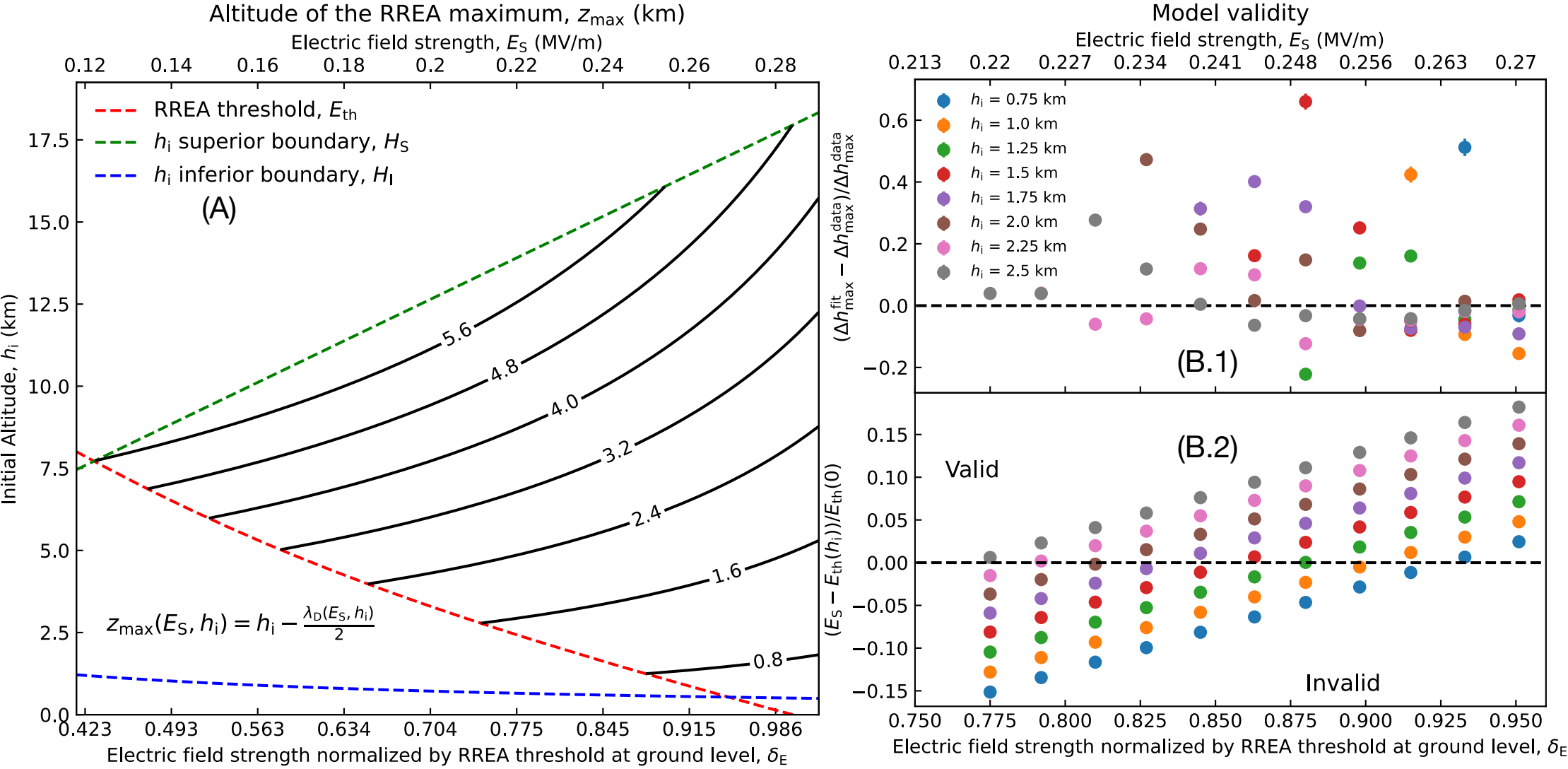
Altitude of the RREA maximum, z_{max} (km)
Electric field strength, E_S (MV/m)
0.12
0.14
0.16
0.18
0.2
0.22
0.24
0.26
0.28
RREA threshold, E_{th}
h_i superior boundary, H_S
h_i inferior boundary, H_I
(A)
5.6
4.8
4.0
3.2
2.4
1.6
0.8
$z_{max}(E_S, h_i) = h_i - \frac{\lambda_D(E_S, h_i)}{2}$
Initial Altitude, h_i (km)
0.0
2.5
5.0
7.5
10.0
12.5
15.0
17.5
0.423
0.493
0.563
0.634
0.704
0.775
0.845
0.915
0.986
Electric field strength normalized by RREA threshold at ground level, δ_E
Model validity
Electric field strength, E_S (MV/m)
0.213
0.22
0.227
0.234
0.241
0.248
0.256
0.263
0.27
h_i = 0.75 km
h_i = 1.0 km
h_i = 1.25 km
h_i = 1.5 km
h_i = 1.75 km
h_i = 2.0 km
h_i = 2.25 km
h_i = 2.5 km
$(\Delta h_{max}^{fit} - \Delta h_{max}^{data})/\Delta h_{max}^{data}$
0.6
0.4
0.2
0.0
−0.2
(B.1)
(B.2)
Valid
Invalid
$(E_S - E_{th}(h_i))/E_{th}(0)$
0.15
0.10
0.05
0.00
−0.05
−0.10
−0.15
0.750
0.775
0.800
0.825
0.850
0.875
0.900
0.925
0.950
Electric field strength normalized by RREA threshold at ground level, δ_E